Dynamics of dissociative attachment of electrons to water through the $^2B_1$ metastable state of the anion

Daniel J. Haxton,[1,2,*] Zhiyong Zhang,[2,†] Hans-Dieter Meyer,[3,‡]
Thomas N. Rescigno,[2,§] and C. William McCurdy[4,5,1,¶]

[1] *Department of Chemistry, University of California, Berkeley, California 94720*
[2] *Lawrence Berkeley National Laboratory, Computing Sciences, Berkeley, California 94720*
[3] *Theoretische Chemie, Universität Heidelberg, Im Neuenheimer Feld 229, D - 69120 Heidelberg, Germany*
[4] *Lawrence Berkeley National Laboratory, Chemical Sciences, Berkeley, California 94720*
[5] *Department of Applied Science, University of California, Davis, California 95616*

Calculations of cross sections for dissociative attachment to water through the $^2B_1$ resonance state are presented using the *ab initio* surfaces calculated previously for the energy, E_R, and width, Γ, of this resonance state as a function of nuclear geometry. The dynamics of the dissociative attachment process are treated in full dimensionality using the local complex potential model. For the $H^- + OH$ channel, the calculations presented here are in substantial agreement with experiment with regard to total cross section and vibrational excitation of the OH fragment. Cross sections for dissociative attachment to excited initial ro-vibrational states are presented and isotope effects are also examined.

I. INTRODUCTION

Experiments[1–8] on the dissociative attachment of electrons to gas-phase water molecules have suggested that this process is governed by complex nuclear and electronic dynamics. Three resonance peaks have been identified with cross section maxima near incident electron energies of 6.4, 8.4, and 11.2 eV for the production of the H^-, O^- or OH^- products. It was observed that each of these peaks exhibits a different product distribution. The three electronic resonance states corresponding to these three cross section peaks, with $^2B_1$, $^2A_1$ and $^2B_2$ symmetry, are now familar, and it is the dynamics of dissociative attachment through the lowest of those, the $^2B_1$ metastable state of the anion, that is the subject of this paper.

Several salient features of the early experiments suggest that the nuclear dynamics of this process may hold some surprises. For dissociative attachment through the $^2B_1$ resonance, the cross section for producing $H^- + OH$ is roughly 40 times larger at its peak than the cross section for producing the energetically favored products, $O^- + H_2$ [4, 5]. The further observation that the production of OH^- associated with this resonance peak in these early experiments was not a product of direct dissociative attachment [9] is contrary to the natural chemical intuition from the condensed phase that OH^- should be expected to be a major product. These observations indicate that the products of this reaction are determined by the dynamics of the process itself rather than by the energetics of the possible product channels, and that moreover those dynamics are different for each of the resonance states of the water anion.

Both the detailed experiments of Belič, Landau and Hall [8] in 1981, who measured the distribution of vibrational states of OH as well as angular distributions of the accompanying H^-, and those of Compton and Christophorou [4], who measured the isotope effect for production of H^- or D^- from H_2O or D_2O, provide strong tests of the theoretical understanding of this process. The channel producing $H^- + OH$ through the $^2B_1$ resonance state is accompanied by extensive vibrational excitation of the OH fragment. Given the competition between dissociation channels and the observed product vibrational excitation, one expects that the dynamics of dissociative attachment to this molecule are intrinsically polyatomic, and can only be described theoretically by a treatment using the full dimensionality of nuclear motion. Such a treatment is what we report here.

In a previous paper [10], hereafter refered to as (**I**), we presented the calculation of the potential surface for the $^2B_1$ resonance state in its full dimensionality. That surface, $V = E_R - i\Gamma/2$, is complex in the region in which this state is metastable. Both the real part and the width, Γ, were calculated by *ab initio* methods, the real part in large-scale configuration interaction calculations and the width from complex Kohn variational scattering calculations. Analytic fits of these quantities were performed to construct a complete representation at all geometries necessary for the dynamics calculations we describe here.

In this study we turn to the calculation of the cross sections for dissociative attachment using that complex potential surface. The calculations we present are all peformed using the local complex potential model [11–14], in which the energy and width of the resonance state are sufficient to determine the nuclear dynamics and the cross sections.

To apply the local complex potential model to a polyatomic system, we make use of a time-dependent version of it that simplifies both the numerical calculations

* djhaxton@lbl.gov
† zyzhang@lbl.gov
‡ dieter@tc.pci.uni-heidelberg.de
§ tnrescigno@lbl.gov
¶ cwmccurdy@lbl.gov

and the physical interpretation of the dynamics. As in earlier studies on resonant vibrational excitation of CO_2 [15, 16], we make use of the Multiconfiguration Time Dependent Hartree (MCTDH) method [17] to solve the working equations. This time-dependent approach, combined with the power of the MCTDH implementation, is the key to treating polyatomic dissociative attachment and resonant vibrational excitation problems.

The outline of this paper is as follows. In Section II we discuss the bulk of the formalism involved in this work: essentials of the local complex potential model, relevant definitions of dissociative attachment cross sections, the coordinate systems and Hamiltonians necessary for the treatment of a triatomic system, and the application of the MCTDH method to the computation of the quantities of interest. In Section III we present our results, and conclude with the discussion in Section IV. An Appendix is included in which we address the analysis of the rotational degree of freedom for the OH fragment of the H^- + OH channel, which is not straightforward.

II. TIME-DEPENDENT LOCAL COMPLEX POTENTIAL TREATMENT OF DISSOCIATIVE ATTACHMENT

A. Nuclear wave equation

The local complex potential (LCP) model [11–14, 18] , also known as the "Boomerang" model when applied to vibrational excitation, describes the nuclear dynamics in terms of the driven Schrödinger equation

$$(E - H)\,\xi_{\nu_i}(\vec{q}) = \phi_{\nu_i}(\vec{q}, 0), \tag{1}$$

in which the Hamiltonian for nuclear motion in the resonant state is

$$H = K_{\vec{q}} + E_R(\vec{q}) - \frac{i\Gamma(\vec{q})}{2}. \tag{2}$$

In Eqs. (1-2), the nuclear degrees of freedom are collectively denoted by $\vec{q}$ and the nuclear kinetic energy is denoted by $K_{\vec{q}}$. The energy, E, is the energy of the entire system, namely that of the target molecular state plus the kinetic energy of the incident electron,

$$E = E_{\nu_i} + k^2/2. \tag{3}$$

The driving term, ϕ_{ν_i} in Eq. (1), is defined as

$$\phi_{\nu_i}(\vec{q}, 0) = \sqrt{\frac{\Gamma(\vec{q})}{2\pi}}\chi_{\nu_i}(\vec{q}). \tag{4}$$

in which χ_{ν_i} is the initial vibrational wave function of the neutral target molecule, whose quantum numbers are collectively denoted by ν_i. The factor which multiplies χ_{ν_i}, called the "entry amplitude," is arrived at via certain approximations [11–14]. As we will see below, the magnitude of the driving term ϕ_{ν_i} will largely control the overall magnitude of the cross section.

The solution of Eq. (1) can be accomplished via time-dependent methods, as first demonstrated by McCurdy and Turner [19]. The solution $\xi_{\nu_i}(\vec{q})$ satisfies the boundary condition that it should contain only purely outgoing waves,

$$\xi_{\nu_i}(\vec{q}) = (E - H + i\epsilon)^{-1}\phi_{\nu_i}(\vec{q}, 0). \tag{5}$$

By representing the Green's function, $(E - H + i\epsilon)^{-1}$, by the Fourier transform of the corresponding propagator, the stationary solution $\xi_{\nu_i}(\vec{q})$ of Eq. (1) can be obtained,

$$\begin{aligned}\xi_{\nu_i}(\vec{q}) &= \lim_{\epsilon\to 0}\; i\int_0^\infty e^{i(E+i\epsilon)t}e^{-iHt}\phi_{\nu_i}(\vec{q}, 0)dt \\ &= \lim_{\epsilon\to 0}\; i\int_0^\infty e^{i(E+i\epsilon)t}\phi_{\nu_i}(\vec{q}, t)dt,\end{aligned} \tag{6}$$

where we define the time-dependent nuclear wave function as

$$\phi_{\nu_i}(\vec{q}, t) = e^{-iHt}\phi_{\nu_i}(\vec{q}, 0). \tag{7}$$

The essence of the LCP model is that the dynamics of this wavepacket on the complex potential surface of the metastable anion determine the cross sections for dissociative attachment (DA) or vibrational excitation through the electron scattering resonance. These wavepacket dynamics provide a simple interpretation of the physics of the dissociative attachment process that is now well-known for diatomics, but, as we will see below, is even more useful for understanding dissociative attachment to polyatomic targets.

The LCP model is expected to describe the dynamics of the case at hand well, since certain basic assumptions of the model are clearly satisfied [20]. Our interest here is in describing DA to water, whose electronic ground state at equilibrium has $^1A_1$ symmetry, through its lowest resonance anion state, which at the equlibrium geometry of the neutral target has $^2B_1$ symmetry. This resonance lies ∼6.5 eV above the neutral target state. The width of the resonance, and therefore the coupling of the resonance state to the background electron scattering continuum, is small, and the incident electron energy is large compared to the vibrational spacing of the neutral molecular target.

Virtually all previous *ab initio* studies of dissociative electron attachment have been carried out for diatomics, or for polyatomics with a single active nuclear degree of freedom. In such cases the quantum numbers l and m of the initial state are conserved via the approximations which yield Eq. (4), and therefore the coordinates, $\vec{q}$, reduce to a single internuclear distance, R. The radial portion of the wave function given in Eq. (5), defined as Ξ,

$$\xi_{lm\nu}(R, \theta, \phi) = Y_{lm}(\theta, \phi)\Xi_{l\nu}(R), \tag{8}$$

behaves asymptotically as an outgoing wave:

$$\Xi_{l\nu}(R) \underset{R\to\infty}{\longrightarrow} \exp(i\kappa R - il\pi/2)A_l(E_{l\nu} + \frac{k^2}{2}). \quad (9)$$

The total cross section for dissociative attachment in the local complex potential model is then [21],

$$\begin{aligned}\sigma_{DA} &= \frac{2\pi^2}{k^2} g \frac{\kappa}{\mu_R} \lim_{R\to\infty} |\Xi_{l\nu}(R)|^2 \\ &= \frac{2\pi^2}{k^2} g \frac{\kappa}{\mu_R} \left| A_l(E_{l\nu} + \frac{k^2}{2}) \right|^2 ,\end{aligned} \quad (10)$$

where κ is the relative nuclear momentum of the two atoms with reduced mass μ_R, and g is a statistical ratio of the electronic multiplicity of the resonant state to the electronic multiplicity of the incoming state.

The generalization of this formulation to polyatomic systems is, in principle, straightforward. However, there are intrinsic complications that arise even in the simplest polyatomic case of a triatomic molecule, because there is more than one final arrangement channel. We therefore must first specify the coordinate systems and Hamiltonians which we will employ, before addressing the issue of the proper formulation of the dissociative attachment problem for a triatomic.

B. Jacobi coordinate systems

A three-body system has nine degrees of freedom; nine variables are required to specify the configuration of such a system in space. Three of these variables, however, describe center-of-mass motion, which can easily be separated from internal motion. The instantaneous positions of three particles define a plane, so of the remaining six variables, three can be chosen to specify motion in this plane, while the remaining three are used to orient the plane with respect to the space-fixed frame. There are several possible choices for the three internal (body-fixed) coordinates that describe motion in a plane. We will use Jacobi coordinates, which are a natural choice for studying dissociation.

There are two distinct Jacobi coordinate systems that describe a triatomic system such as H_2O. In the first of these we define an OH bond length, r, the distance, R, between that OH center of mass and the second H, and the angle, γ, between these two vectors, defined such that $\gamma = 0$ corresponds to a collinear H-H-O geometry. The other coordinate system considers H_2 as the diatomic species and thus assigns r to the H-H separation, and R to the distance between the H_2 center of mass and and the oxygen nucleus, with γ defined as the angle between these two vectors. These coordinate systems were described in (**I**) when the construction of analytic fits of the calculated *ab initio* complex potential surface were discussed.

The calculations described below made use of both coordinate systems so that the cross sections for different arrangements could be computed. The first Jacobi coordinate system is convenient for the OH + H^- arrangement channel; the second, for the the H_2 + O^- arrangement channel.

The remaining three degrees of freedom of this center-of-mass system are the three Euler angles which orient the internal or body-fixed (BF) frame to the lab or space-fixed (SF) frame, which we will denote α, β, ζ. These are shown in Figure 1 and will be discussed below.

C. Triatomic nuclear Hamiltonians

The angular momentum of a triatomic system can be quantized in several different ways. In defining the Hamiltonian for this system we will use the standard [22] BF formulation in which we quantize total angular momentum, J, the projection of angular momentum onto a SF axis, M, and the projection upon a BF axis, K. J and M are constants of the motion. A six-dimensional rovibrational wave function for a triatomic with particular J and M values can be expanded in a BF angular momentum basis as follows,

$$\Psi^{JM}(R, r, \gamma, \alpha, \beta, \zeta) = \sum_{K=-J}^{J} \widetilde{D}^J_{MK}(\alpha, \beta, \zeta) \frac{\Xi^{JM}_K(R, r, \gamma)}{Rr} \quad (11)$$

where the basis of $\widetilde{D}^J_{MK}(\alpha, \beta, \zeta)$ is the set of normalized Wigner rotation matrices (and BF angular momentum eigenstates),

$$\widetilde{D}^J_{MK}(\alpha, \beta, \zeta) = \sqrt{\frac{2J+1}{8\pi^2}} D^J_{MK}(\alpha, \beta, \zeta), \quad (12)$$

such that

$$\begin{aligned}\int_0^{2\pi} d\alpha \int_{-1}^{1} d(\cos\beta) \int_0^{2\pi} d\zeta \widetilde{D}^J_{MK}(\alpha, \beta, \zeta) \widetilde{D}^{J'*}_{M'K'}(\alpha, \beta, \zeta) \\ = \delta_{J,J'}\delta_{M,M'}\delta_{K,K'}.\end{aligned} \quad (13)$$

In Eqs.(12) and (13) we follow the conventions of Zhang [22], which for the D^J_{MK} are the same as those of Edmonds [23].

By substituting the expansion (11) into the Schrödinger equation and using the orthogonality relation (13) for the D-functions, one can derive a tridiagonal system of coupled equations for the radial components, $\Xi^{JM}_K(R, r, \gamma)$, of the full wave function. The BF Hamiltonian operators that appear in this expansion

are given by [24, 25]

$$
\begin{aligned}
H^J_{KK} &= -\frac{1}{2\mu_R}\frac{\partial^2}{\partial R^2} - \frac{1}{2\mu_r}\frac{\partial^2}{\partial r^2} + \frac{\hat{j}^2}{2\mu_r r^2} \\
&\quad + \frac{1}{2\mu_R R^2}[J(J+1) - 2K^2 + \hat{j}^2] \\
&\quad + V(R,r,\gamma) \\
H^J_{K\pm1,K} &= -\frac{1}{2\mu_R R^2}\sqrt{J(J+1) - K(K\pm1)}\,\hat{j}_\pm \\
\hat{j}^2 &= -\left(\frac{1}{\sin(\gamma)}\frac{\partial}{\partial\gamma}\sin(\gamma)\frac{\partial}{\partial\gamma} - \frac{K^2}{\sin^2(\gamma)}\right) \\
\hat{j}_\pm &= \mp\frac{\partial}{\partial\gamma} - K\cot(\gamma),
\end{aligned}
\tag{14}
$$

where μ_r and μ_R are the reduced masses appropriate for the Jacobi coordinate system in use and V is the complex potential energy surface. The Hamiltonian operators are, of course, independent of the SF quantum number, M. Thus the dynamics in the body-fixed frame are effectively four-dimensional, with internal coordinates r, R, and γ, and with the expansion in terms of states of fixed K representing the fourth dimension.

We use the "R-embedding" scheme [26] in which the BF angular momentum number K is quantized around the axis parallel to the R vector. Thus α and β are the polar angles which orient the R vector with respect to the SF frame, and ζ is the third Euler angle specifying orientation about the BF z axis. A schematic of the coordinate system is shown in Fig. 1.

With this Hamiltonian, in the Jacobi coordinates appropriate to the final arrangement of interest, we can perform the time propagation of Eq. (7), expanding the initial wave function ϕ_{ν_i} as in Eq. (11). With the understanding that the wave function being propagated corresponds to a specific value of total angular momentum, we will drop the J and M superscripts on the wave function for notational simplicity. Before we turn to the methods we will use to perform that time propagation, we will generalize the definition of the dissociative attachment cross section in Eq. (10) using these coordinates.

D. Dissociative attachment cross sections

We can now address the problem of generalizing Eq. (10), which expresses the cross section for dissociative electron attachment to a diatomic target, to the case of a triatomic system. The definition of the cross section derives from the asymptotic form of the time-independent solution, ξ_{ν_i}, of the driven Schrödinger equation in the LCP model given by Eq. (1). Here and below, we use the subscript ν_i to denote the quantum numbers that specify the initial state of the target molecule. For the product channels, consisting of an atom or atomic ion plus a diatomic fragment, we will use the notation $j\nu$ to label the vibrational and rotational quantum numbers of the product diatom.

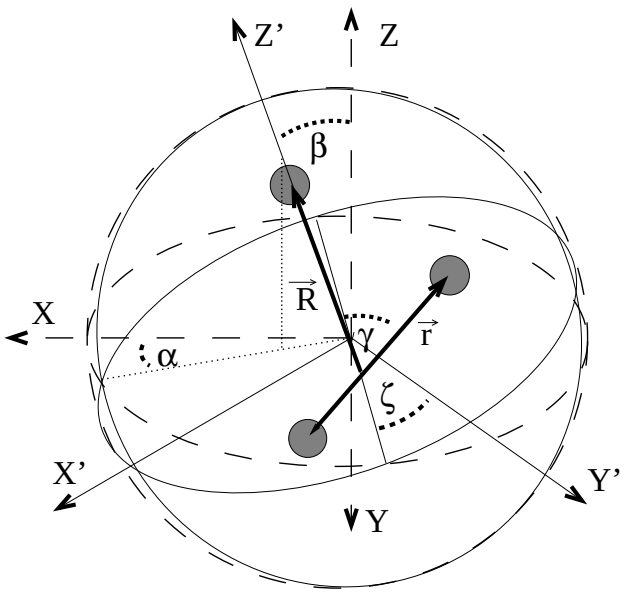

FIG. 1: "R-embedding"[26] coordinate system with origin at the center of mass. The body-fixed (BF) frame is labeled by the X', Y', and Z' axes; the space-fixed (SF), by X, Y, and Z. The BF axes are marked with thin lines, and the BF $X'Z'$ and $X'Y'$ planes are both marked with a thin line circle. The SF axes are marked with dashed lines, and the SF XZ and XY planes are marked with dashed circles. The molecule resides in the BF $X'Z'$ plane. The Euler angles α, β, and ζ orient the BF frame with respect to the SF frame. The line of nodes is also drawn. The $\vec{r}$ vector connects the nuclei of the diatomic. The $\vec{R}$ vector connects the center of mass of the diatomic to the third atom and is collinear with the BF Z' axis. R is the length of $\vec{R}$, r is the length of $\vec{r}$, and γ is the angle between the $\vec{R}$ and $\vec{r}$ vectors.

For the triatomic case, the asymptotic form of $\xi_{\nu_i}(\vec{R},\vec{r})$ is expressed most easily in the spaced-fixed basis of coupled spherical harmonics $\mathscr{Y}^{JM}_{jl}(\hat{R},\hat{r})$, where $\hat{R}\cdot\hat{r} = \cos(\gamma)$. The quantum numbers l and j, as we will see below, label the partial-wave angular momentum of the dissociating fragments and the rotational quantum number of the diatomic product, respectively.

For our purposes, an important identity is the definition of the coupled spherical harmonics in terms of the normalized Wigner rotation functions [22],

$$
\mathscr{Y}^{JM}_{jl}(\hat{R},\hat{r}) = \sum_K C^{JK}_{lj}\,\tilde{D}^J_{MK}(\alpha,\beta,\zeta)\Theta^K_j(\gamma) \tag{15}
$$

where the coefficients C^{JK}_{lj} of this unitary transformation are given in terms of Clebsch-Gordon coefficients by

$$
C^{JK}_{lj} = \sqrt{\frac{2l+1}{2J+1}}\langle jKl0|JK\rangle, \tag{16}
$$

and

$$
\Theta^K_j(\gamma) \equiv \sqrt{2\pi}Y_{jK}(\gamma,0). \tag{17}
$$

For a total energy of $E = E_{\nu_i} + k^2/2$, where k is the wavenumber of the incident electron and E_{ν_i} is the energy

of the initial state, the asymptotic form of the dissociative attachment wave function, written below in the space-fixed frame, is that of a purely outgoing wave:

$$\begin{aligned}\xi^{SF}_{\nu_i}(\vec{R},\vec{r}) &= \sum_{lj\nu} f^{+}_{l\nu_i j\nu}(R)\chi_\nu(r)\frac{\mathscr{Y}^{JM}_{jl}(\hat{R},\hat{r})}{Rr} \\ &\underset{R\to\infty}{\longrightarrow} \sum_{lj\nu}\exp(i\kappa_{j\nu}R - il\pi/2)\chi_\nu(r)\times \\ &\quad \frac{\mathscr{Y}^{JM}_{jl}(\hat{R},\hat{r})}{Rr}A_{lj\nu}(E_{\nu_i}+\frac{k^2}{2}),\end{aligned} \tag{18}$$

where $A_{lj\nu}(E_{\nu_i}+\frac{k^2}{2})$ is a partial-wave DA amplitude. The relative momentum associated with the separating fragments is

$$\kappa_{j\nu} = \sqrt{2\mu_R\left(E_{\nu_i}+\frac{k^2}{2}-E_{j\nu}\right)}, \tag{19}$$

where $E_{j\nu}$ is the energy of the diatomic rovibrational state with quantum numbers ν and j of the rearrangement channel in question.

Given the expansion of the dissociative attachment wave function in Eq. (18), the generalization of the cross section formula for diatomics in Eq. (10) to a triatomic is straightforward. We begin by taking the overlap of ξ_{ν_i} with the final product states of interest and integrating over the remaining angular degrees of freedom:

$$O_{j\nu}(R) = R^2\sum_K\left|\left(\frac{\chi_\nu}{r}\widetilde{D}^J_{MK}\Theta^K_j\middle|\xi^{SF}_{\nu_i}\right)\right|^2, \tag{20}$$

where $\chi_\nu(r)$ is a vibrational state of the diatomic product and Θ^K_j, defined in Eq. (17), is a corresponding rotational state of the diatomic fragment. The curved brackets indicate integration over all variables except R. In principle χ_ν also depends on the rotational quantum number, j. However, in the calculations we report here, no centrifugal term was included in the vibrational potential for the diatomic fragment, for reasons that will be made clear below; hence χ has no j subscript here.

The quantity $O_{j\nu}(R)$ is fully analagous to the quantity $|\Xi_{l\nu}(R)|^2$ of Eq. (10), and we therefore define the cross section for dissociative attachment to a triatomic as

$$\sigma^{j\nu}_{DA} = \lim_{R\to\infty}\frac{2\pi^2}{k^2}g\frac{\kappa}{\mu_R}O_{j\nu}(R). \tag{21}$$

By using the asymptotic expansion given by Eq. (18), we obtain the expression

$$\sigma^{j\nu}_{DA} = \frac{2\pi^2}{k^2}g\frac{\kappa}{\mu_R}\sum_l\left|A_{lj\nu}(E_{\nu_i}+\frac{k^2}{2})\right|^2. \tag{22}$$

The rotational states of the products are not resolved in most experiments, so to compare with measured DA cross sections we will generally be interested in computing the rotationally summed DA cross sections.

E. The Multiconfiguration Time-Dependent Hartree Method

As previously stated, the solution of the time-independent LCP equation (1) can be accomplished by time-dependent wavepacket propagation methods. We will first give a brief description of the MCTDH method we used to carry out the time propagation and then, in the following subsection, show how the dissociative attachment cross section, defined above in Eq. (22), is calculated directly from the time-propagated wavepacket.

To perform the propagation in Eq. (7) we use the Heidelberg MCTDH package [27], which is an implementation of the Multi–Configuration Time–Dependent Hartree, or MCTDH [17, 28–30] method. The MCTDH method has proven its utility in many applications (see Ref. [17] and references therein) as an efficient adaptive method for nuclear dynamics of molecular systems – in particular, those with many degrees of freedom [31–33].

In the MCTDH method, as in the standard method for solving the time-dependent Schrödinger equation, we start with a time-independent orthonormal product basis set,

$$\{\chi^{(1)}_{j_1}(q_1)...\chi^{(f)}_{j_f}(q_f)\}, \qquad j_\kappa = 1\cdots N_\kappa \tag{23}$$

for a problem with f degrees of freedom and nuclear coordinates labeled $q_1,...q_f$. For computational efficiency, the basis functions $\chi^{(\kappa)}_{j_\kappa}$ are chosen as the basis functions of a discrete variable representation (DVR) [34].

The central idea of the MCTDH technique is the representation of the nuclear wavepacket as a sum of separable terms,

$$\phi_{\nu_i}(\vec{q},t) = \sum_{j_1=1}^{n_1}\cdots\sum_{j_f=1}^{n_f}A_{j_1\ldots j_f}(t)\prod_{\kappa=1}^{f}\varphi^{(\kappa)}_{j_\kappa}(q_\kappa,t), \tag{24}$$

with $n_\kappa \ll N_\kappa$. Each "single particle function" (or SPF) $\varphi^{(\kappa)}_{j_\kappa}(q_\kappa,t)$ is itself represented in terms of the primitive basis:

$$\varphi^{(\kappa)}_{j_\kappa}(q_\kappa,t) = \sum_{i_\kappa=1}^{N_\kappa}c^{(\kappa)}_{i_\kappa j_\kappa}(t)\chi^{(\kappa)}_{i_\kappa}(q_\kappa). \tag{25}$$

Since both the coefficients $A_{j_1\ldots j_f}$ and the single-particle functions $\varphi^{(\kappa)}_{j_\kappa}$ are time-dependent, the wave function representation is not unique. Uniqueness can be achieved by imposing additional constraints on the single-particle functions which keep them orthonormal for all times [17].

The size of the SPF expansion in Eq. (24) controls the degree to which correlation among the various degrees of freedom is included. Including a greater number of terms in this expansion leads to a more precise but slower calculation. Including the maximum number, i.e. $n_\kappa = N_\kappa$, gives a numerically exact calculation, while the opposite limit $n_\kappa = 1$ yields the Time-Dependent Hartree (TDH) method [35, 36] in which the propagating wavepacket is

uncorrelated with respect to the coordinate system chosen to represent it.

As the single–particle functions are time–dependent, matrix elements of the Hamiltonian have to be evaluated at every time step. Hence it is essential that this evaluation can be done quickly. A fast algorithm exists [17, 29] if the Hamiltonian can be written as a sum of products of single–coordinate operators. Here the kinetic energy operator is – as usual – already in product form, but the potential energy surface is not. To profit from the advantages of the product form we approximate the potentials employed as a sum of separable terms, i.e.,

$$V(q_1, \cdots q_f) \approx \sum_{j_1=1}^{m_1} \cdots \sum_{j_f=1}^{m_f} C_{j_1 \cdots j_f} v_{j_1}^{(1)}(q_1) \cdots v_{j_f}^{(f)}(q_f). \quad (26)$$

The MCTDH package [27] includes a utility which performs a fit of a given potential to a separable representation of this form. Details can be found in Beck *et al.*[17]. All potential energy surfaces used in the current calculation were represented in this manner, using this utility to fit them specifically for each choice of the DVR grids.

F. Dissociative Attachment Cross Sections from Outgoing Projected Flux

The cross sections for dissociative attachment, given by Eq. (22), can be calculated directly from the time-propagated wavepacket by computing the energy-resolved, outgoing projected flux. The energy resolution is achieved by Fourier transform and a final state resolution is achieved by the introduction of appropriate projection operators. For DA leading to a specific rovibrational final product, we use the projection operator

$$P_{j\nu} = \sum_K \left| \frac{\chi_\nu}{r} \widetilde{D}^J_{MK} \Theta^K_j \right\rangle \left\langle \frac{\chi_\nu}{r} \widetilde{D}^J_{MK} \Theta^K_j \right|, \quad (27)$$

while for the case of the rotationally summed DA cross sections, we use the operator

$$P_\nu = \left| \frac{\chi_\nu}{r} \right\rangle \left\langle \frac{\chi_\nu}{r} \right|. \quad (28)$$

The flux operator we employ, which measures the flux passing through a surface defined by $R = R_c$, is defined as

$$\hat{F} = i[H, h(R - R_c)] \quad (29)$$

where h is a heaviside function. The energy-resolved projected flux is then given by

$$F_{j\nu}(E) = \frac{1}{2\pi} \int_0^\infty dt \int_0^\infty dt' \langle \phi_{\nu_i} | e^{i(H-E)t} P_{j\nu} \hat{F} P_{j\nu} e^{-i(H-E)t'} | \phi_{\nu_i} \rangle \quad (30)$$

The MCTDH package [27] includes a utility which computes the outgoing projected flux. In the actual calculations, the flux operator appearing in the equation above is replaced by a Complex Absorbing Potential (CAP)[37–39]. This formulation of the flux operator is very convenient numerically and entirely equivalent to the traditional formal definition of the operator in this context. The radius R_c is to be interpreted as the point where the CAP is switched on. For more details on this CAP flux formalism see Refs. [17, 30, 40].

The resulting energy-resolved projected flux is that associated with the time-independent solution of the driven Schrödinger equation of the LCP model in Eq. (1),

$$F_{j\nu}(E) = \frac{1}{2\pi} \langle \xi_{\nu_i} | P_{j\nu} \hat{F} P_{j\nu} | \xi_{\nu_i} \rangle. \quad (31)$$

By inserting the expansion of ξ_{ν_i} in Eq. (18) into Eq. (31) and using the properties of the coupled spherical harmonics defined in Eqs.(15-17), we obtain, after some algebra,

$$F_{j\nu}\left(E_{\nu_i} + \frac{k^2}{2}\right) = \sum_l \frac{1}{2\pi} \langle f^+_{l\nu_i j\nu}(R) | \hat{F} | f^+_{l\nu_i j\nu}(R) \rangle. \quad (32)$$

Then using the asymptotic form of the radial continuum functions $f^+_{l\nu_i j\nu}(R)$, some further manipulation gives

$$F_{j\nu}\left(E_{\nu_i} + \frac{k^2}{2}\right) = \sum_l \left| A_{lj\nu}\left(E_{\nu_i} + \frac{k^2}{2}\right) \right|^2 \left(\frac{\kappa_{j\nu}}{2\pi\mu_R}\right). \quad (33)$$

This equation gives us the desired relationship between the energy-resolved projected outgoing flux and the amplitudes for dissociation that appear in the asymptotic form of the wave function in Eq. (18. By comparing Eq. (33) and (22), noting that in this case $g = 1$, the relationship between the rotationally and vibrationally resolved total dissociative attachment cross section and the energy-resolved projected flux, $F_{j\nu}$, is found to be

$$\sigma^{j\nu}_{DA}\left(\frac{k^2}{2}\right) = \frac{4\pi^3}{k^2} F_{j\nu}\left(E_{\nu_i} + \frac{k^2}{2}\right). \quad (34)$$

Similarly, for the rotationally summed DA cross section, we use:

$$\sigma^{\nu}_{DA}\left(\frac{k^2}{2}\right) = \frac{4\pi^3}{k^2} F_{\nu}\left(E_{\nu_i} + \frac{k^2}{2}\right), \quad (35)$$

where F_ν is defined as in Eq. (31), with $P_{j\nu}$ replaced by P_ν. These formulas were used to compute cross sections using the MCTDH method. For the H^- + OH channel, an additional factor of two is multiplied into this expression to account for the fact that in a given calculation we perform the flux analysis for only one of the two H^- + OH arrangements, namely the one for which the Jacobi coordinates are appropriate.

III. COMPUTATIONAL PROCEDURES

A. The DVR basis and other MCTDH parameters

In the calculations reported here we used DVR primitive basis sets for all internal degrees of freedom [17], choosing the standard sine DVR for the r and R degrees of freedom and, for $J = 0$, the Legendre DVR for γ. For $J > 0$, the DVR for γ must be modified to account for singularities in the Hamiltonian (see Eq. 14) due to the term $K^2/\sin^2(\gamma)$. This is done by using an extended Legendre DVR [41, 42], which is implemented in the Heidelberg MCTDH package [27].

Most of the results we will report are for rotationally summed cross sections and it is for these cases that the following computational details apply. For the case of rotationally resolved final states, there are additional considerations that come into play; the details of the rotational analysis we used are described in the Appendix. In the Jacobi $r = r_{OH}$ coordinate systems, we obtained convergence with DVR bases of $70\times120\times40$ for $(0.5 < r < 7.0)$, $(0.0 < R < 12.0)$, and $(0 < \gamma < \pi)$, respectively. For this coordinate system, with the exception of the calculation incorporating an initial state with one quantum of asymmetric stretch, the convergence of the calculation with respect to the number of single particle functions was relatively slow compared, for example, to our earlier studies on vibrational excitation of a triatomic [15, 16]. Therefore we used a large SPF expansion, $24\times28\times18$ in r, R, γ, to attain converged results. For consistency, this SPF expansion was used for all calculations presented in this paper performed in this Jacobi coordinate system.

We also performed a few calculations in the Jacobi $(r = r_{HH})$ coordinate system, to examine the $H_2 + O^-$ channel. We used a grid of $0.5 < r < 9.0$, $0.0 < R < 9.0$, and $0 < \gamma < \pi$ with DVR order $90\times90\times60$ in an attempt to calculate the total cross section only. For these calculations, which each took two to three days CPU time on a desktop computer, an SPF expansion of $24\times29\times26$ in r, R, γ was used. As we will discuss below, these calculations gave only an estimate of the total cross section for the production of O^-, and cannot be considered to have been converged.

For every propagation, we used complex absorbing potentials (CAPs) [37–39] at the edge of the grid to eliminate the propagated wave function before reaching the end of the grid. In all cases our CAP's began 3 bohr before the end of the grid, were quadratic, and had a strength, η in the notation of ref. [17], of 0.007au. Formally, the CAP's provide the $+i\epsilon$ limit in Eq. (6).

B. Initial states

To investigate the effect of excitation of the water molecule on dissociative attachment, we performed calculations using various initial rovibrational states. We also calculated a few of these initial states using the spectroscopically accurate ground-state surface of Polyanski, Jensen and Tennyson [43], denoted here and by those authors as the PJT2 surface, for the purpose of verifying the quality of the initial states obtained from the ground state CI surface calculated in (**I**), which we denote here as the HZMR surface.

Vibrational states of H_2O can be denoted by the notation (n_1,n_2,n_3), where n_1 is the quantum number of symmetric stretch, n_2 is the quantum number of bend, and n_3 is the quantum number of asymmetric stretch. For the Jacobi $(r = r_{OH})$ coordinate system, we obtained and used initial states as follows: for $J = 0$, the (000), (100), (010), (001), and (200) states, both for D_2O and H_2O; for $J = 3$, we studied the 7 lowest rovibrational states of H_2O; and for $J = 10$, we studied the ground rovibrational state of H_2O. To calculate initial rovibrational states, we performed improved relaxation [30] with a Davidson diagonalizer as implemented in the MCTDH package [27].

Table I lists all initial states used for our calculations on H_2O. We computed the overlap of vibrational states from the HZMR surface and three corresponding states we obtained by improved relaxation using the PJT2 surface. As shown in Table I these overlaps are nearly unity. In Table I we also present comparisons of our calculated transition energies with values calculationed by Polyanski *et al.* [43] and by Carter and Handy [44] and with experimental values. In the course of investigating the two different arrangement channels for this problem, we calculated two of these transition energies in both distinct Jacobi coordinate systems, $r = r_{OH}$ and $r = r_{HH}$, and Table I also compares these results. Together, these tests verify that any error in the cross sections we calculate here due to errors in the initial rovibrational wave functions is negligible.

Vibrational states for $J = 0$ for H_2O, integrated over $\cos\theta$ in valence coordinates, are shown in Fig. 2. This figure shows the probability density of each wave function in the (r_1, r_2) plane in valence-bond coordinates. The (000) and (010) wavefunctions appear nodeless in this figure, though of course (010) has a node in θ, and they are almost indistinguishable here, although the (010) state is shifted slightly in the symmetric stretch direction. The (100) state has a node parallel to the asymmetric stretch direction, and is elongated in the symmetric stretch direction; conversely, the (001) state has a node along $r_1 = r_2$ and is elongated in the asymmetric stretch direction.

C. Propagation

The initial states obtained from the HZMR surface were multiplied by the entrance amplitude and propagated using the MCTDH procedure discussed above. Propagation was performed for 75 fs (H_2O) or 100 fs (D_2O) after which 99.9% of the density had typically been either absorbed by the CAP or by the imaginary

State				Energies				Overlap
J	K_a	K_c	Vib.	Present (HZMR)	Present (PJT2)	Calc.	Expt.	$\|\langle$PJT2$\|$HZMR$\rangle\|^2$
0	0	0	(000)	0.0 cm^{-1}	0.0 cm^{-1}	0.0 cm^{-1}	–	0.9975
0	0	0	(010)	1635.85[a]	1594.63[a]	1594.68[c]	1594.7[e]	0.9974
				1635.93[b]				
0	0	0	(020)	3219.95[b]		3151.53[c]	3151.6[e]	
0	0	0	(100)	3745.06[a]	3657.05[a]	3657.15[c]	3657.1[e]	0.9923
0	0	0	(001)	3805.78[a]		3755.83[c]	3755.93[e]	
0	0	0	(200)	7366.35 [a]		7202.23[c]	7201.5[e]	
3	0	3	(000)	138.78[a]		136.9[d]	136.8[f]	
3	1	3	(000)	144.16[a]		142.4[d]	142.3[f]	
3	1	2	(000)	175.82[a]		173.6[d]	173.4[f]	
3	2	2	(000)	208.80[a]		206.3[d]	206.3[f]	
3	2	1	(000)	214.82[a]		212.2[d]	212.2[f]	
3	3	1	(000)	288.26[a]		284.9[d]	285.2[f]	
3	3	0	(000)	288.47[a]		285.1[d]	285.4[f]	
				288.41[b]				
10	0	10	(000)	1129.85[a]				

[a] From calculation in Jacobi ($r = r_{OH}$) coordinates
[b] From calculation in Jacobi ($r = r_{HH}$) coordinates
[c] From Polyansky, Jensen and Tennyson [43]
[d] From Carter and Handy [44]
[e] As quoted in [43]
[f] As quoted in [44]

TABLE I: Initial states for H_2O from the present calculations on both the HZMR and PJT2 surfaces compared with other calculated and experimental results. The quantum numbers K_a and K_c are defined as in references [43, 44].

component of the resonance surface. A time-step plot of the wave function density for a packet beginning with attachment to the (000) state with $J = 0$ is shown in Fig.3 and will be discussed further below.

IV. RESULTS AND DISCUSSION

A. Cross sections for attachment to the ground vibrational state with $J = 0$

The experimental determinations of dissociative attachment to water in the gas phase with which we compare here have been performed at low enough effective temperatures that the target molecule is in its ground vibrational state. To compare with those measurements, we performed LCP calculations using the methods described above beginning with the (000) state and with $J = 0$. As we will see below, rotational excitation has only a very small effect on the cross sections, at least up to $J = 10$, so these calculations are appropriate for comparison with the experiments which have been performed to date. These calculations yielded a total cross section for the $OH + H^-$ channel (summed over final rotational and vibrational states of the OH fragment) which peaks at 6.81eV incident electron energy with a value of $0.214a_0^2$ or 5.99 $\times 10^{-18}$ cm^2 and which has an energy-integrated total cross section of 5.74×10^{-18} eV cm^2.

Our computed cross sections for various final vibrational states are shown in the top panel of Fig. 4 and are compared with the experiments of Belić, Landau and Hall[8] in Fig. 5. The value of the total cross section at its peak nearly reproduces the experimental value of 6.4×10^{-18}cm^2 and displays a shape very similar to the experimental one, with the calculated maximum being shifted slightly from the experimental maximum at an incident energy of 6.5 eV. A similar level of vibrational excitation of the OH fragment is observed, with similar magnitudes. However, as is visible in Fig. 5, there are increasing quantitative discrepancies for the cross sections as ν increases from 0 to 7 and the cross sections decrease by two orders of magnitude. This level of agreement with experiment suggests that the potential surface from (**I**) is largely correct, at least for the geometries relevant to the description of the H^- + OH channel, and that the dynamics of the wavepacket shown in Fig. 3 are the origin of the extensive vibrational excitation of the product OH fragment.

As described in (**I**) and as is apparent in Fig. 2, in the vicinity of the equilibrium geometry of the neutral ($r_1 = r_2 = 1.81$ bohr; $\theta = 104.5°$) the gradient of the real part of the resonance energy is steeply downhill in the r_1 or r_2 directions. In contrast, the potential is relatively flat in θ. The $H_2 + O^-$ well can only be reached if

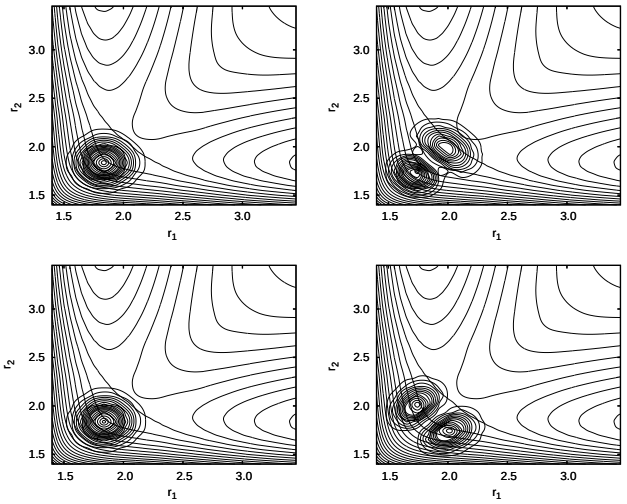

FIG. 2: Initial wave function density for radial solution of (clockwise, from upper left) (000), (100), (001), and (010) states, in valence-bond coordinates, integrated over cos θ, with real part of $^2B_1$ surface at $\theta = 104.5°$. Distances in bohr; contours every 0.25eV.

the bond angle θ is decreased substantially from the equilibrium geometry of the neutral, whereas the OH + H^- channel is immediately adjacent to the initial wavepacket. Therefore, the wavepacket proceeds downhill towards the OH + H^- arrangement channel, with very little density arriving in the H_2 + O^- well.

Since the wavepackets for both ground and vibrationally excited initial wavepackets begin high upon the repulsive wall of the resonant state, they all initially acquire a large amount of momentum in the symmetric stretch direction, which becomes vibrational and translational motion in the H^- + OH wells. This effect is seen clearly in Fig. 3 as the oscillation of the outgoing packet in the exit wells of the potential surface. This dynamics is the origin of vibrational excitation in the product fragment, and it is one of the central qualitative results of this study of the dynamics of dissociative attachment through the $^2B_1$ resonance.

Dissociative attachment through the $^2B_1$ state is also characterized by rotational excitation of the OH fragment in these calculations. In Figure 7 we plot rotational distributions for the ground vibrational state, $\nu = 0$, and the $\nu = 4$ state of OH, for attachment to the ground state of water. These results were obtained via projections onto hindered-rotor or "pendular" states using an extended potential energy surface, as described in the Appendix. Some structure is seen in these cross sections, although for the reasons discussed in the Appendix, these distributions may be suspect for $j < 4$ or so.

The experiments of Belič, Landau and Hall [8] cite a maximum in the rotational distribution at $j = 7$ for the $\nu = 0$ state and $j = 4$ or 5 for $\nu = 4$, but those authors did not report values of individual cross sections for rotational excitation. The present results are consistent with the results of these experiments to the extent that they predict considerable rotational excitation of the OH fragment in this channel. A detailed comparison is not possible, and there is some uncertainty in the experiment, but it seems that the maximum in the calculated final rotational distribution may be different from that observed experimentally and the calculations seem to show somewhat greater overall rotational excitation.

B. Effects of initial rotational and vibrational excitation

In our calculations, initial rotational excitation had a very little effect on the cross sections for dissociative attachment. In Fig. 8 we plot the total cross section for the OH + H^- channel obtained from the calculation on the $J = 0$ (000) initial state, along with cross sections from rotationally excited initial states. The curves in that figure are almost indistinguishable, suggesting that the cross sections for $J = 0$ should therefore be essentially identical to the values for a thermally averaged population of rotational states at the effective temperatures of the experiments.

On the other hand, initial vibrational excitation of the target molecule can affect the cross sections in the OH + H^- channel dramatically and in ways that are very much mode-specific, as can be seen in Figs. 4 and 6. For example, one quantum of bend excitation, (010), has only a small effect the cross sections, while a single quantum of excitation in asymmetric stretch, (001), changes the degree of vibrational excitation in the products significantly, as is shown in Fig. 4.

Due to the node in the $r_1 = r_2$ direction for the (001) state as shown in Fig. 2, the dynamics for this initial wavepacket are such that the bifurcating wavepacket moves more directly down the H-OH wells and therefore results in significantly less vibrational excitation than for attachment to the other states examined. While this result indicates some of the mode specificity of the effects of vibrational excitation, the initial states with quanta of symmetric-stretch excitation provide the most dramatic example of mode-specific behavior observed in these calculations.

As seen in Fig. 6, the cross sections for dissociative attachment to the (100) initial state has a strong minimum near an incident electron energy of 6.5 eV, esentially independent of the final vibrational state of the products. The value of the total cross section at this minimum is $0.0014 a_0^2$, compared to its peak value of $0.21 a_0^2$ at 5.89eV. This behavior is reminiscent of an effect [45] predicted for photodissociation of water through the $^1B_1$ state. The $^{1,3}B_1$ states both correspond to the configuration which is the parent of the $^2B_1$ resonance state, and in the region in which the initial vibrational state is nonzero they have potential energy surfaces which are similar in shape to that of the resonance state.

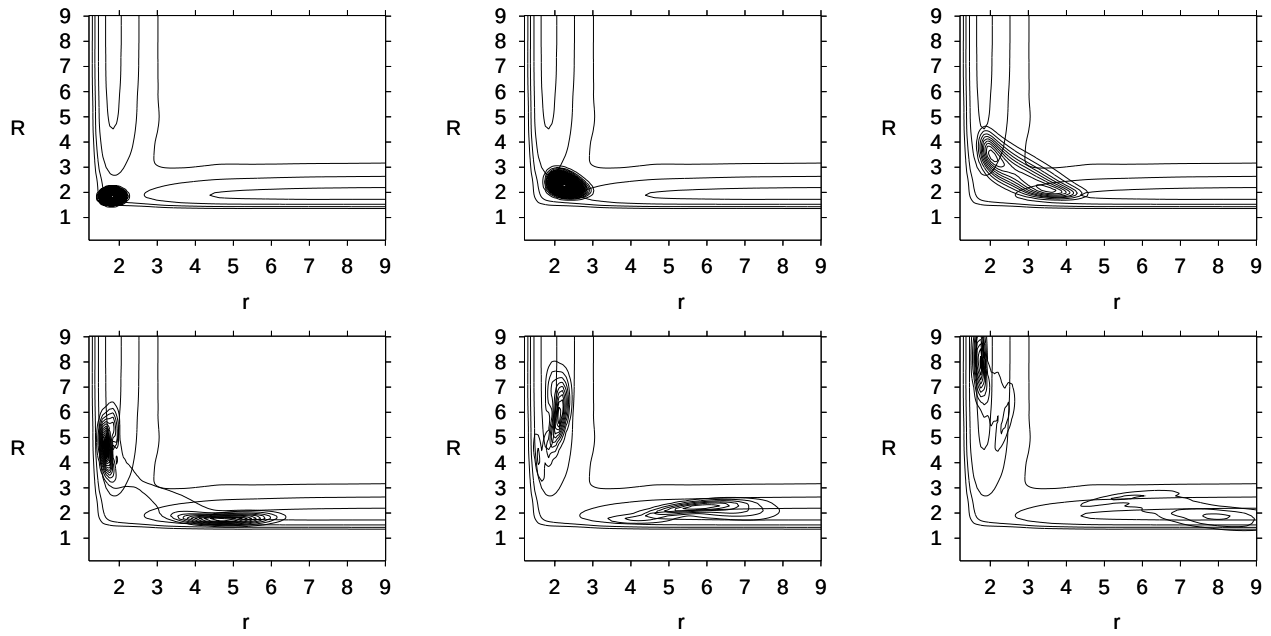

FIG. 3: Radial wave function probability density for propagation of (000) initial state, in Jacobi ($r = r_{OH}$) coordinates, integrated over $\cos\gamma$, at t =0, 4, 8, 12, 16, and 20 fs. Also shown is the real part of resonant surface at $\gamma = 108°$, which most closely corresponds to $\theta = 104.5°$ at equilibrium geometry, with contours every 1eV. Distances in bohr.

In either dissociative attachment or photodissociation of a *diatomic* molecule such an effect would be simple to explain. The amplitude for dissociative attachment for a diatomic molecule can be written in a form equivalent to that appearing in Eq. (10) so that it is proportional to the matrix element $\langle\psi_E^-|\Gamma^{1/2}|\chi_{\nu_i}\rangle$, where $\psi_E^-(R)$ is the scattering wave function for atom-atom scattering on the potential surface of the resonance. This form is of course reminiscent of the matrix element for the photodissociation amplitude. If the initial vibrational wave function $\chi_{\nu_i}(R)$ has a node, and we make the simple delta function approximation for ψ_E^- at the classical turning point, we can see that at some energy this matrix element will be zero. If there are two nodes in χ_{ν_i}, this effect will occur at two energies.

In a polyatomic system a similar argument can be used, although the geometry of the multidimensional wave functions makes it more complicated because no single coordinate corresponds to the dissociation motion near the Franck-Condon region. The effect here is essentially polyatomic. Nonetheless, the similarity of the present case of dissociative attachment to water initially excited in the symmetric stretch mode to the case of photodissociation is further underscored by the cross section for the (200) initial state shown in Fig. 6. Here we see two minima, as the simplest explanation would predict from the presence of two nodes in the wave function of the initial vibrational state, and multiple minima are also seen in calculations on photodissociation of water [45].

C. Isotope effects

The experimental cross sections for $D^- + OD$ and $H^- + OH$ show pronounced isotope effects. Compton and Christophorou [4] have observed that not only does the $D^- + OD$ cross section exhibit a lower peak maximum than does the H_2O cross section, but also a smaller peak width, and thus a significantly smaller energy-integrated cross section.

In Figs. 9 and 10 we plot cross sections for dissociative attachment to D_2O for $J = 0$ beginning in the (000), (100), (010), (001), and (200) states. The calculated isotope effects evident in these figures can be summarized collectively as follows. In the cross sections for the various initial states of D_2O, we observe narrower peaks than for H_2O. We observe higher maxima at the peak values for the D_2O cross sections, and energy-integrated cross sections with about the same values as those for the corresponding processes in H_2O. We also observe onsets at higher energy for D_2O initial states, due to the fact that the lower energes of the initial states for the heavier isotope result in a larger incident electron energy being required to access the resonant surface. Compton and Christophorou [4] found energy-integrated cross sections of 6.6 and 3.9×10^{-18} eV cm^2 for H_2O and D_2O, respectively, and peak heights of 6.9 and 5.2 $\times10^{-18}$ cm^2. We find integrated cross sections of 5.79 and 5.33×10^{-18} eV cm^2 and peak heights of 5.99 and 7.04 $\times10^{-18}$ cm^2 for H_2O and D_2O, respectively.

Thus, the salient differences between our calculations and experimental observations is that our peak heights

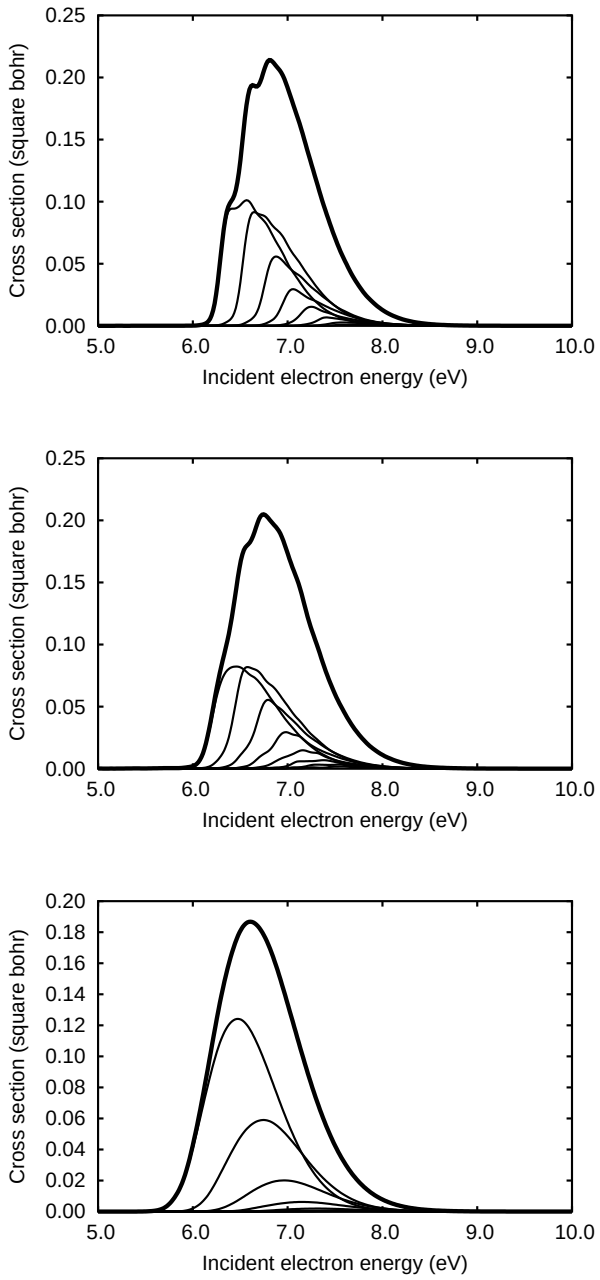

FIG. 4: Total cross sections for (top to bottom) (000), (010), and (001) initial states for $J = 0$ H_2O, along with projections into each final vibrational state of OH; channels which have onsets left to right with increasing ν.

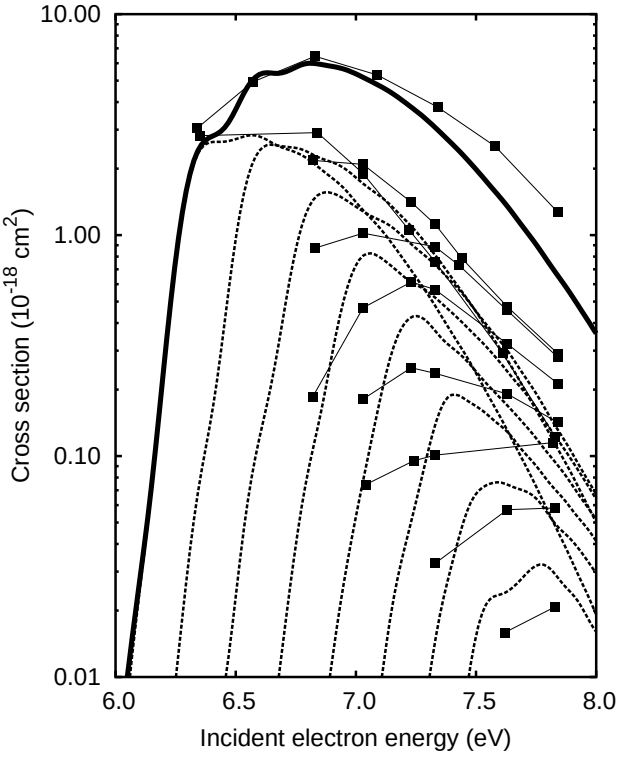

FIG. 5: Cross sections for (000) initial state, total (heavy line) and into vibrational channels $\nu = 0$ through $\nu = 7$ of OH (dotted lines, left to right), on a logarithmic scale. Also included is data from Belìc, Landau and Hall's[8] measurements (thin lines with squares), shifted in energy so that the maxima (present, 6.81eV, versus their value of 6.5eV) in the total cross section coincide.

for the D_2O cross sections are larger, not smaller, than for H_2O, and our energy-integrated cross sections have nearly the same value for the two isotopomers.

These results are puzzling, especially in light of the fact that the calculated isotope effects are what are to be expected if there is negligible autodetachment during the dissociation process. Due to the small width of this resonance, as calculated in (**I**) and by others [46, 47], only one or two percent of the propagated wave function density is lost to autodetachment in our wavepacket calculations. The expected isotope effect is particularly evident if we first think about the process as though it occurred in one dimension. In that case the semiclassical "reflection principle", in which one makes the approximation that the continuum function for dissociation is a delta function at the classical turning point, results in the shape of the cross section being determined by the shape of the initial wavepacket, $\chi_{\nu_i}\sqrt{\Gamma/2\pi}$. Because the initial vibrational wave function for the heavier isotope is more sharply peaked and narrower, we expect to see D_2O cross sections which are also more strongly peaked and narrower than those for H_2O. In more than one dimension these arguments are complicated by the fact that no single coordinate maps simply from the Franck-Condon region inhabited by the initial states of the molecule to the asymptotic region, but the results are qualitatively the same as for a diatomic.

Compton and Christophorou [4] were entirely aware of these arguments and explained the observed isotope effects by invoking a much larger rate of autodetachment than is suggested by modern *ab initio* calculations of the

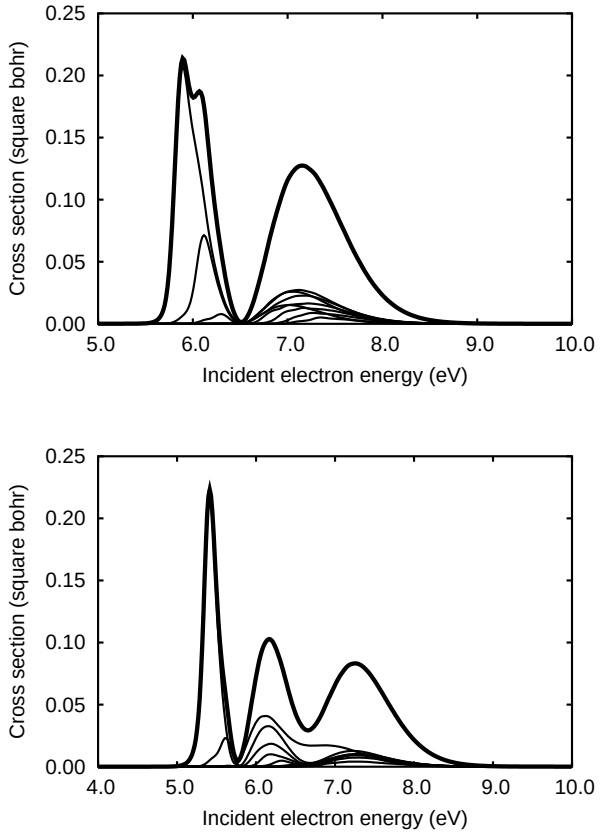

FIG. 6: Total cross sections from (100) initial state (top) and (200) initial state (bottom) for $J = 0$ H_2O, along with projections into each final vibrational state of OH; channels which have onsets left to right with increasing ν.

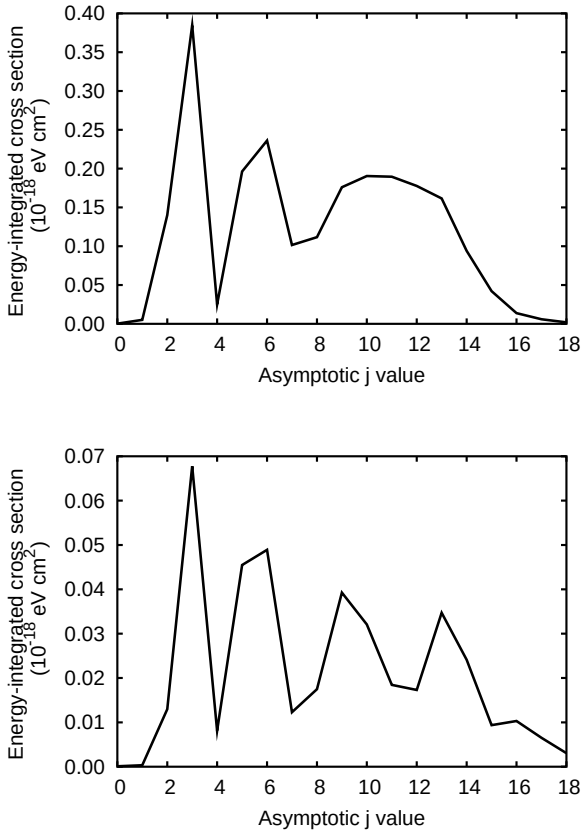

FIG. 7: Rotational distribution for $\nu = 0$ (top) and $\nu = 4$ (bottom) final vibrational states of H_2O as obtained from a calculation on the $J = 0$ (000) initial state using the extended potential energy surface. The energy-integrated cross section for each of the rotational/vibrational states is plotted with respect to j value.

width of the $^2B_1$ state. They argued that since in the deuterium case the dissociation process takes longer, a large autodetachment probability would lead to a smaller cross section for dissociative attachment in the case of D_2O. In this way they derived a lifetime of 2.1×10^{-14} seconds, which corresponds to a width of approximately $\Gamma = 0.197$eV.

Unfortunately, the LCP model indicates that a width of this magnitude would yield much larger cross sections via its effect on the entry amplitude. Increasing the width in our calculations so as to match the isotope effect yields cross sections that are several times those of the experiments of Belič, Landau and Hall. Increasing the width further so that autodetachment dominates and finally reduces the cross section back to near the experimental values exagerates the isotope effect far beyond that observed by Compton and Christophorou. To quantify this assertion we repeated the ground-state H_2O and D_2O calculations with widths multiplied by several factors; at 27 times the original width, the cross sections are approximately 10 times those we calculated originally. Somewhere between 9 and 27 times our calcu-

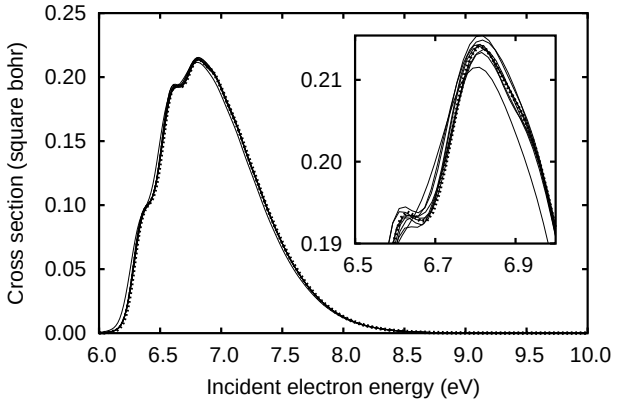

FIG. 8: Total cross sections in square bohr for rotationally excited initial states. The heavy dotted line is for $J = 0$ (000) initial state; the other lines are for the first seven rovibrational states for $J = 3$, which are very close to the $J = 0$ line, and the ground state for $J = 10$, which is slightly farther away.

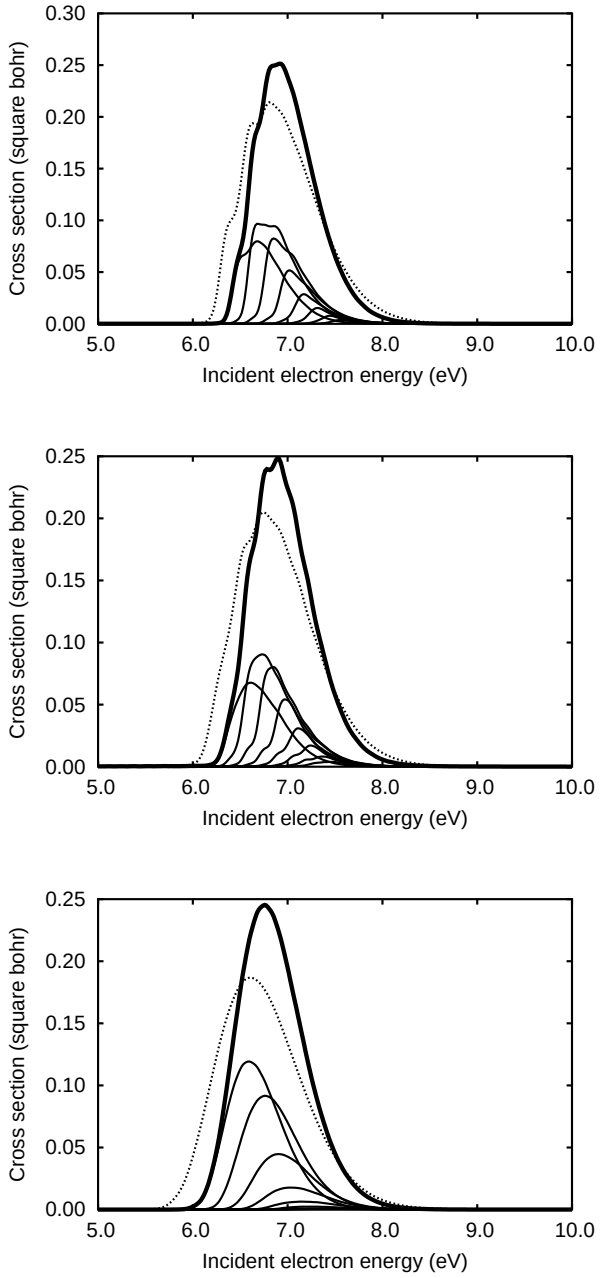

FIG. 9: Total cross sections for (000), (010), and (001) initial states for D_2O, $J = 0$, along with cross sections for production of vibrationally excited OD, which have onsets left to right with increasing ν. Also plotted as the dotted lines are the total cross sections for the corresponding H_2O initial states.

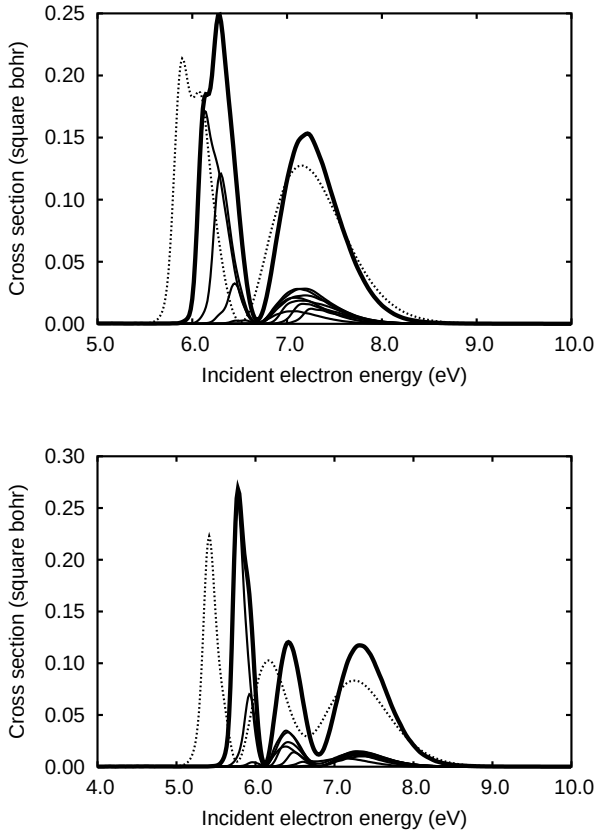

FIG. 10: Total cross sections for (100) and (200) initial states (top and bottom, respectively) for D_2O, $J = 0$ along with cross sections for production of vibrationally excited OD, which have onsets left to right with increasing ν. Also plotted as the dotted lines are the total cross sections for the corresponding H_2O initial states.

lated width we find that the isotope ratio (in terms of energy-integrated cross section) agrees with experiment. For larger widths, where autodetachment dominates dissociative attachment and cross sections have returned to the magnitude observed in experiment, the isotope effect is much larger – indicating a factor of three difference between the energy-integrated cross sections of H_2O and D_2O. Thus, we are not able to reproduce the experimentally observed isotope effects and overall magnitude of the cross section by simply adjusting the magnitude of the calculated width.

However, we can speculate about the possible ways in which we may have failed to reproduce physical effects leading to the experimentally observed isotope effect. There are two qualitatively different mechanisms through which an isotope effect like that observed in experiment could be obtained, while still maintaining the overall magnitude of the cross sections observed and calculated in this study.

In the first of these, the form of the entrance amplitude, $\sqrt{\Gamma/2\pi}$, may preferentially weight portions of the Franck-Condon region in which the initial H_2O wavefunction has a significantly larger magnitude than that of the corresponding D_2O wavefunction. As a result, the driving term ϕ_{ν_i} of Eq. (1) may have a larger magnitude for the H_2O states than for the corresponding D_2O states,

and as a result the energy-integrated cross section will be larger for the H_2O state. However, some investigation into this mechanism revealed it to be highly implausible. In spite of the large difference in the reduced masses for the vibrational motion of these isotopomers, the initial wavefunctions for corresponding states are actually not very different. In a harmonic oscillator approximation, the ground-state vibrational wavefunctions are Gaussians with standard deviations in the ratio $1{:}2^{1/4} = 1{:}1.18$ for $D_2O{:}H_2O$. Thus, the entrance amplitude would have to be extremely sharply peaked to account fully for the observed isotope effect. We observe no such radical structure in the entrance amplitude, and such extreme behavior would be such a deviation from the results of this study, and every other study of the widths of negative ions of which we are aware, as to be extremely implausible.

The second mechanism which we have examined is much more reasonable, given the calculations which we describe in (**I**). As explained in that paper, we have obtained the width Γ, which appears in both the entrance amplitude and as the imaginary component of the potential energy surface of the resonant state, exclusively in terms of calculations at which the location of the resonance does not exceed the energy of its parent $^1B_1$ state. Thus, in the construction of the imaginary component of the resonance energy we have disregarded any partial width of the resonant state due to autodetachment to an excited state of the neutral water molecule. However, as we note in (**I**), there are many geometries at which the Complex Kohn calculations place the resonance above its parent. These geometries lie beyond the Franck-Condon region – in particular, at geometries in which one O-H bond length is increased from the equilibrium geometry of the neutral. These geometries lie at the entrance of the $OH + H^-$ well. We note that the Complex Kohn calculations in (**I**) employed a basis set optimized for the description of the resonance state and the ground state of the neutral water molecule, not for the excited states of the neutral, and thus may actually have placed the resonance even lower than it should be relative to the neutral excited states. As a result, we consider it a possibility that the resonance may actually rise above not only its $^3B_1$ parent state but also some or all of the $^1B_1$, $^1A_1$, or $^3A_1$ states as it enters the $OH + H^-$ well and thus acquire a large negative imaginary component to its energy at these geometries. Model calculations indicate that such an increase in the width would have to be large – on the order of 0.05eV or so – to duplicate the experimentally observed isotope effects. However, this is the only mechanism of which we are aware that could account for these results.

D. Dissociative attachment into the $O^- + H_2$ Channel

The experimental value of the cross section for production of O^- through the $^2B_1$ resonance at its peak is about 40 times smaller than the peak of the cross section for production of H^- through the same resonance [5]. The dynamics on the potential surface computed in (**I**) presented here are consistent with that result to the extent that H^- is by far the dominant channel in our calculations.

As we pointed out in (**I**), although the $H_2 + O^-$ exit well includes the lowest points on the potential energy surface, it is not as immediately accessible from ground-state equilibrium geometry as is the $OH + H^-$ well. The steepest descent path of the potential energy surface does in fact lead from equilibrium geometry into the $O^- + H_2$ well, but via a more indirect path (described in (**I**)) than the path to the $H^- + OH$ channel. Thus in the competing dynamics for the wavepacket to exit into these two arrangements, the more direct path to the production of H^- dominates, and the wavepacket has essentially all exited into that channel (with its two equivalent arrangements) before more than a small amount of the quantum flux begins to move into the channel producing O^-. Thus, the dynamics of the wave packet in the LCP model shows it is the shape of the potential surface and not the overall energetics that controls the branching ratio into the two possible arrangement channels for anion production.

Unfortunately, the *ab initio* potential surface computed in (**I**)) seems to over estimate this effect. We were not able to completely converge the calculations in this channel, but preliminary indications are that the surface from (**I**) produces cross sections about one order of magnitude smaller than experiment for this channel. As these calculations were not converged, we attempted no final state analysis for this channel.

V. SUMMARY

The results we have presented here demonstrate that it is now possible to perform completely *ab initio* calculations on dissociative attachment to a triatomic molecule in full dimensionality. Such calculations require almost the complete arsenal of contemporary techniques of first-principles quantum chemistry and chemical dynamics, and would have been difficult to obtain, even with today's powerful computers, without the MCTDH implementation of the wavepacket dynamics in the time-dependent version of the LCP model.

These calculations have achieved substantial agreement with experimental observation in many respects. The magnitude of the observed total cross section for the $H^- + OH$ channel has been reproduced to within less than ten percent, and the degree of vibrational excitation of the OH fragment calculated is very similar to that ob-

served. The OH fragment is also produced in these calculations with considerable rotational excitation, as in the experiment, although the degree of rotational excitation is probably exaggerated in the present calculations.

The dominance of the production of H^- over that of O^- is also confirmed by these calculations, and most importantly, the combination of the dynamics presented here and the potential surface presented in (**I**) explain why this channel dominates dissociative attachment through the $^2B_1$ resonance. We speculate that the reason why we understimate the cross section into the O^- channel is that the *ab initio* surface computed in (**I**) does not represent the resonance potential energy surface in the region between the $H^- + OH$ and $H_2 + O^-$ wells accurately enough to correctly represent the minor channel in a dynamical competition that yields the observed branching ratio of 40 to 1.

Considerable additional work will be necessary to completely unravel the dynamics of dissociative attachment to water. Besides refining the understanding gained in this study of attachment through the $^2B_1$ resonance state using a still better *ab initio* potential surface, similar studies must be undertaken for the $^2A_1$ and $^2B_2$ resonances seen in the original experiments on this problem. The questions of nonadiabatic couplings between these states and its effect on branching ratios remain open as well. Since the understanding of radiation damage to biological systems will require a complete understanding of this most fundamental process and how it is modified in the liquid phase and by the proximity of biomolecules, this problem will continue to be a principal target of experiment and theory in the near future.

Acknowledgments

This work was performed under the auspices of the US Department of Energy by the University of California Lawrence Berkeley National Laboratory under Contract DE-AC03-76SF00098 and was supported by the U.S. DOE Office of Basic Energy Sciences, Division of Chemical Sciences. HDM gratefully acknowledges support through the "DFG Forschergruppe: Schwellenverhalten, Resonanzen und nichtlokale Wechselwirkungen bei niederenergetischen Streuprozessen".

APPENDIX: ROTATIONAL ANALYSIS

The practical necessity of carrying out wavepacket propagation on finite grids of limited range can cause problems when long-range forces come into play. That is the case here when we consider the computation of DA cross sections for rotationally specific final states. The rotational analysis for the $H^- + OH$ channel is complicated by the fact that this channel contains a long-range potential corresponding to the interaction of a polar diatomic molecule and an ion, a potential which is significant for all geometries on our grid. The analysis of the rotational degree of freedom for the OH fragment must therefore be performed in terms of hindered-rotor or "pendular" states, not free rotational states. (A previous discussion of pendular states can be found in Ref.[48].) From the point in R at which we perform this analysis, the pendular states are assumed to connect adiabatically with the free rotational states of the asymptotic region. In other words, we assume that the cross sections which we compute for the jth pendular state correspond to the cross sections observed in experiment for the jth free rotational state. We describe a test of this assumption below.

The long-range ion-dipole interaction causes mixing among the rotational and, in principle, also the vibrational levels of the product states. However, since the dipole moment of OH is almost constant with bond length, and the separation between vibrational levels is very large compared to the ion-dipole interaction, the mixing between vibrational states caused by motion in γ or R should be very small.

On the other hand, the separation between the pendular states is relatively small. Hence, there will be coupling among these pendular states caused by motion in the R degree of freedom. Therefore, in order to perform a meaningful rotational analysis, we were required to ensure that this coupling be small enough not to induce nonadiabatic transitions between pendular states as they progress beyond the edge of our grid. To this end we extended our potential energy surface beyond the boundary at $R = 12$ that we used for the other calculations presented here. We computed additional points on the potential surface using the methods of (**I**) at $R = 16$ and 24 bohr and extended our surface to 24 bohr so that we could place the CAP at $R = 21$.

As described in (**I**), the procedure by which we construct the real part of the resonance surface incorporates both an analytic fit and a 3D cubic spline of the difference between the analytic fit and the computed points. In order to optimize our surface for the rotational analysis, we computed a new 3D spline representation of the entire surface using the following analytic fit of the $H^- + OH$ potential well:

$$\begin{aligned} V_{H-OH}(r,R,\gamma) = & \\ & -0.69746\cos(\gamma)/R^2 - 38.349\cos^2(\gamma)/R^4 + \\ & 0.1652\left(\left(1-\exp[1.2971\,(1.8112-r)]\right)^2 - 1\right), \end{aligned} \tag{A.1}$$

which was obtained from a multidimensional fit of the *ab initio* calculated points at $R > 11$, $r < 4$. The pendular states with respect to which the rotational analysis was performed are the eigenfunctions of the hindered rigid rotor Hamiltonian, $\hat{j}^2/2\mu_r r^2 + V$, using for V the first two terms in the potential in Eq. (A.1) with $R = 22.0$ and with $r^2 = \langle r^2 \rangle_\nu$ for the vibrational state of OH in question. The pendular states thus have a parametric dependence on R and ν.

In order to verify that the nonadiabatic couplings between pendular states were in fact small by the edge of

our recomputed and extended grid, we performed a calculation on an analogous model problem to compute sample nonadiabatic couplings between pendular states. We approximated the dissociating H^- + OH channel as a rigid static dipole in the field of the H^- ion. We thus defined an R-dependent adiabatic pendular state basis $\Theta_j(\gamma;R)$ as eigenfunctions of the Hamiltonian

$$H_{adiabatic}(\gamma;R) = \frac{1}{2\mu_r\langle r^2\rangle}\hat{j}^2 + \frac{A}{R^2}\cos(\gamma) \qquad \text{(A.2)}$$

with eigenvalue $\epsilon_j(R)$, i.e.

$$H_{adiabatic}\Theta_j(\gamma;R) = \epsilon_j(R)\Theta_j(\gamma;R). \qquad \text{(A.3)}$$

We took the dipole moment A and expectation value $\langle r^2\rangle$ of the OH molecule to be that computed from the first vibrational state of OH by a 1D wavefunction relaxation using the results of a CI calculation performed on the OH molecule. The dipole moment from that calculation was A = -1.658 Debye, and $\langle r^2\rangle$=3.497. The coupling between the pendular states is caused by the nuclear kinetic energy in the R direction in the full Hamiltonian for this rigid dipole-ion pair,

$$H_{full} = H_{adiabatic} - \frac{1}{2\mu_R}\frac{\partial^2}{\partial R^2}. \qquad \text{(A.4)}$$

The adiabatic potentials $\epsilon_j(R)$ are combined with the nonadiabatic couplings to produce the effective Hamiltonian in the R degree of freedom, which can be written in matrix form as

$$\begin{aligned} H_{jj'} &= \delta_{jj'}\left(\epsilon_j(R) - \frac{1}{2\mu_R}\frac{\partial^2}{\partial R^2}\right) \\ &+ \langle\Theta_j(\gamma;R)|\frac{1}{2\mu_R}\frac{\partial^2}{\partial R^2}|\Theta_{j'}(\gamma;R)\rangle \\ &+ \langle\Theta_j(\gamma;R)|\frac{1}{2\mu_R}\frac{\partial}{\partial R}|\Theta_{j'}(\gamma;R)\rangle\frac{\partial}{\partial R} \end{aligned} \qquad \text{(A.5)}$$

We computed the pendular states in the basis of the first 40 Legendre polynomials, in order to parallel the 40th order Legendre DVR used in our MCTDH calculations.

The adiabatic potentials $\epsilon_j(R)$ are shown in Fig. 11. Also plotted is the magnitude of the dipole potential, $|\frac{A}{R^2}|$ in Eq. (A.2). As is apparent from this figure, the energies of the pendular states tend to squeeze together around this line. The second derivative coupling is also at a maximum when adjacent pairs are close to this line, but it was found to be negligible (a small fraction of an meV). In contrast, the first derivative coupling is significant for this system, given the large translational kinetic energies (approximately 2eV) of the dissociating H^- + OH system. Assuming an outgoing plane wave ($e^{i\kappa R}$), the quantity $i\kappa$ multiplies the derivative coupling via the $\partial/\partial R$ operator at the very end of Eq. (A.5). Given a translational kinetic energy of $\kappa^2/2\mu_R$ = 2eV, the first derivative coupling is plotted in Fig. 12. As is apparent from comparing this figure to Fig. 11, the first derivative coupling is comparable in magnitude to the separation between pendular states only for the first few pendular states, and drops monotonically with increasing R.

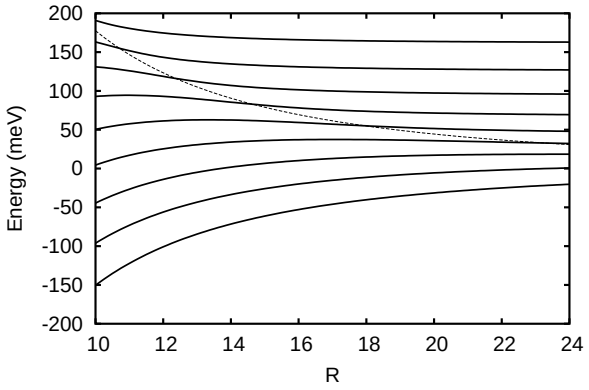

FIG. 11: Diagonal potentials $\epsilon_j(R)$ of the first nine pendular states $\Theta_j(\gamma;R)$ (solid lines). Also plotted for reference is the magnitude of dipole potential $\frac{A}{R^2}$ (dotted line).

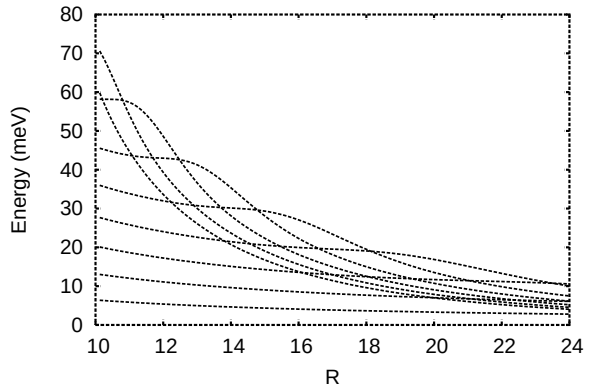

FIG. 12: Absolute value of model nonadiabatic first-derivative coupling between first 9 energetically adjacent pairs of pendular states, assuming $\kappa^2/2\mu_R$ = 2eV.

Given this analysis, we were confident that projections upon pendular states over the region spanned by the CAP, which lies from $R = 21$ to $R = 24$, would yield states that to a good approximation adiabatically change to free rotational states upon continuing farther into the asymptotic region. We expect that this approximation will break down to a significant degree only for the first few rotational states.

[1] W. N. Lozier, Phys. Rev. **36**, 1417 (1930).
[2] I. S. Buchel'nikova, Zh. Eksperim. i Teor. Fiz. **35**, 1119 (1959).
[3] G. J. Schultz, J. Chem. Phys. **44**, 3856 (1966).
[4] R. N. Compton and L. G. Christophorou, Phys. Rev. **154**, 110 (1967).
[5] C. E. Melton, J. Chem. Phys. **57**, 4218 (1972).
[6] S. Trajmar and R. I. Hall, J. Phys. B. **7**, L458 (1974).
[7] M. Jungen, J. Vogt, and V. Staemmler, Chem. Phys. **37**, 49 (1979).
[8] D. S. Belič, M. Landau, and R. I. Hall, J. Phys. B. **14**, 175 (1981).
[9] C. E. Klots and R. N. Compton, J. Chem. Phys. **69**, 1644 (1978).
[10] D. J. Haxton, Z. Zhang, C. W. McCurdy, and T. N. Rescigno, Phys. Rev. A **XX**, XXXX (2004).
[11] D. T. Birtwistle and A. Herzenberg, J. Phys. B **4**, 53 (1971).
[12] L. Dube and A. Herzenberg, Phys. Rev. A **20**, 194 (1979).
[13] T. F. O'Malley and H. S. Taylor, Phys. Rev. **176**, 207 (1968).
[14] T. F. O'Malley, Phys. Rev. **150**, 14 (1966).
[15] T. N. Rescigno, W. A. Isaacs, A. E. Orel, H.-D. Meyer, and C. W. McCurdy, Phys. Rev. A **65**, 032716 (2002).
[16] C. W. McCurdy, W. A. Isaacs, H.-D. Meyer, and T. N. Rescigno, Phys. Rev. A **67**, 042708 (2003).
[17] M. Beck, A. Jäckle, G. Worth, and H.-D. Meyer, Physics Reports **324**, 1 (2000).
[18] J. N. Bardsley and J. M. Wadehra, J. Chem. Phys. **78**, 7227 (1983).
[19] C. W. McCurdy and J. L. Turner, J. Chem. Phys. **78**, 6773 (1983).
[20] A. U. Hazi, T. Rescigno, and M. Kurilla, Phys. Rev. A **23**, 1089 (1981).
[21] W. Domke, Phys. Reports **208**, 97 (1991).
[22] J. Z. H. Zhang, *Theory and Application of Quantum Molecular Dynamics* (World Scientific Publishing Co. Pte. Ltd., 1999).
[23] A. R. Edmonds, *Angular Momentum in Quantum Mechanics* (Princeton University Press, 1996).
[24] C. Petrongolo, J. Chem. Phys. **89**, 1297 (1988).
[25] S. Sukiasyan and H.-D. Meyer, J. Phys. Chem. A **105**, 2604 (2001).
[26] J. Tennyson and B. T. Sutcliffe, J. Chem. Phys. **77**, 4061 (1982).
[27] G. A. Worth, M. H. Beck, A. Jäckle, and H.-D. Meyer, The MCTDH Package, Version 8.2, (2000). H.-D. Meyer, Version 8.3 (2002). See http://www.pci.uni-heidelberg.de/tc/usr/mctdh/.
[28] H.-D. Meyer, U. Manthe, and L. S. Cederbaum, Chem. Phys. Lett. **165**, 73 (1990).
[29] U. Manthe, H.-D. Meyer, and L. S. Cederbaum, J. Chem. Phys. **97**, 3199 (1992).
[30] H.-D. Meyer and G. A. Worth, Theor. Chem. Acc. **109**, 251 (2003).
[31] A. Raab, G. Worth, H.-D. Meyer, and L. S. Cederbaum, J. Chem. Phys. **110**, 936 (1999).
[32] H. Wang, J. Chem. Phys. **113**, 9948 (2000).
[33] H. Wang and M. Thoss, J. Chem. Phys. **119**, 1289 (2003).
[34] J. C. Light, in *Time-Dependent Quantum Molecular Dynamics*, edited by J. Broechkove and L. Lathouwers (Plenum, New York, 1992).
[35] P. A. M. Dirac, Proc. CAmbridge Philos. Soc. **26**, 376 (1930).
[36] A. D. McLachlan, Mol. Phys. **8**, 39 (1964).
[37] C. Leforestier and R. E. Wyatt, J. Chem. Phys **78**, 2334 (1983).
[38] R. Kosloff and D. Kosloff, J. Comput. Phys. **63**, 363 (1986).
[39] U. V. Riss and H. D. Meyer, J. Phys. B **44**, 4503 (1993).
[40] A. Jäckle and H.-D. Meyer, J. Chem. Phys. **105**, 6778 (1996).
[41] G. C. Corey and D. Lemoine, J. Chem. Phys. **97**, 4115 (1992).
[42] J. W. T. G. C. Corey and D. Lemoine, in *Numerical Grid Methods and Their Application to Schrödinger's Equation*, edited by C. Cerjan (Kluwer Academic Publishers, Netherlands, 1973), pp. 1–23.
[43] O. L. Polyansky, P. Jensen, and J. Tennyson, J. Chem. Phys. **105**, 6490 (1996).
[44] S. Carter and N. C. Handy, J. Chem. Phys **87**, 4294 (1987).
[45] R. van Harrevelt and M. C. van Hemert, J. Chem. Phys. **114**, 9453 (2001).
[46] J. D. Gorfinkel, L. A. Morgan, and J. Tennyson, J. Phys. B **35**, 543 (2002).
[47] L. A. Morgan, J. Phys. B **31**, 5003 (1998).
[48] J. Rost, J. Griffin, B. Friedrich, and D. R. Hershbach, Phys. Rev. Lett. **68**, 1299 (1992).